Available online at www.sciencedirect.com
ScienceDirect
Journal of Power Sources 175 (2008) 397–407
JOURNAL OF POWER SOURCES
www.elsevier.com/locate/jpowsour

Local transport phenomena and cell performance of PEM fuel cells with various serpentine flow field designs

Xiao-Dong Wang [a,*], Yuan-Yuan Duan [b], Wei-Mon Yan [c,**], Xiao-Feng Peng [d]

[a] *Department of Thermal Engineering, School of Mechanical Engineering, University of Science & Technology Beijing, Beijing 100083, China*
[b] *Key Laboratory for Thermal Science and Power Engineering of Ministry of Education, Tsinghua University, Beijing 100084, China*
[c] *Department of Mechatronic Engineering, Huafan University, Taipei 22305, Taiwan*
[d] *Laboratory of Phase Change & Interfacial Transport Phenomena, Tsinghua University, Beijing 100084, China*

Received 25 July 2007; received in revised form 2 September 2007; accepted 3 September 2007
Available online 12 September 2007

Abstract

The flow field design in bipolar plates is very important for improving reactant utilization and liquid water removal in proton exchange membrane fuel cells (PEMFCs). A three-dimensional model was used to analyze the effect of the design parameters in the bipolar plates, including the number of flow channel bends, number of serpentine flow channels and the flow channel width ratio, on the cell performance of miniature PEMFCs with the serpentine flow field. The effect of the liquid water formation on the porosities of the porous layers was also taken into account in the model while the complex two-phase flow was neglected. The predictions show that (1) for the single serpentine flow field, the cell performance improves as the number of flow channel bends increases; (2) the single serpentine flow field has better performance than the double and triple serpentine flow fields; (3) the cell performance only improves slowly as the flow channel width increases. The effects of these design parameters on the cell performance were evaluated based on the local oxygen mass flow rates and liquid water distributions in the cells. Analysis of the pressure drops showed that for these miniature PEMFCs, the energy losses due to the pressure drops can be neglected because they are far less than the cell output power.

Keywords: Proton exchange membrane fuel cells; Serpentine flow field; Number of bends; Number of serpentine loops; Flow channel width ratio

1. Introduction

The proton exchange membrane fuel cell is considered to be one of the most promising alternative clean power generators for portable, mobile and stationary applications because of its low to zero emissions, low-temperature operation, high power density and fast start-up. In past decades, numerous fuel cell models have successfully integrated the electrochemical reactions and the transport phenomena [1–23].

The flow field design in the bipolar plates is one of key parameters of a PEMFC, which serves as both the current collector and the reactant distributor. The reactants, as well as the products, are transported to and from the cell through the flow channels. An appropriate flow field design can enhance the reactant transport and the liquid water removal from the cell to minimize the concentration polarization. To this end, various flow field configurations, including parallel, serpentine, interdigitated and many other combined versions, have been developed. Many efforts have been devoted to the optimal flow field design for obtaining high cell performance [11,25–38]. Nguyen [24] designed the interdigitated flow field which forces the reactants to flow through the gas diffusion layer (GDL) with the shear force of this gas flow helping to blow out the liquid water that is entrapped in the inner layers of the electrodes. As a result, the mass transport of the reactants from the flow channel to the inner catalyst layer can be improved and the water flooding at the cathode can be significantly reduced. Cha et al. [25] investigated the PEMFC flow channel scaling behavior with interdigitated, serpentine and spiral interdigitated flow fields. Their results indicated that for most flow pattern archetypes, the optimal feature size occurs at

* Corresponding author. Tel.: +86 10 6232 1277; fax: +86 10 8176 5088.
** Corresponding author. Tel.: +886 2 2663 2102; fax: +886 2 2663 1119.
E-mail addresses: wangxd99@gmail.com (X.-D. Wang), wmyan@huafan.hfu.edu.tw (W.-M. Yan).

0378-7753/$ – see front matter © 2007 Elsevier B.V. All rights reserved.
doi:10.1016/j.jpowsour.2007.09.009

Nomenclature

a	chemical activity of water vapor
A_{cha}	cathode cross-sectional inlet flow area (m^2)
A_{total}	reaction area (m^2)
Aj_0^{ref}	reference exchange current density ($A\,m^{-3}$)
b	source term of variable ϕ
C	mass fraction
C_F	quadratic drag factor
d	hydraulic diameter of the flow channel (m)
D	mass diffusivity ($m^2\,s^{-1}$)
F	Faraday constant (96,487 $C\,mol^{-1}$)
i	current density ($A\,m^{-2}$)
j	current density ($A\,m^{-3}$)
k_c	coefficient of water vapor condensation rate (s^{-1})
k_e	coefficient of water vapor evaporation rate (s^{-1})
k_p	permeability (m^2)
L	distance along the channel measured form the inlet (m)
M	molecular weight ($kg\,mol^{-1}$)
P	pressure (atm)
Q	mass flow rate ($kg\,s^{-1}\,m^{-2}$)
R	universal gas constant (8.314 $J\,mol^{-1}\,K^{-1}$)
s	volume ratio occupied by liquid water
t	time (s)
T	temperature (K)
u	x direction velocity ($m\,s^{-1}$)
v	y direction velocity ($m\,s^{-1}$)
V	fuel velocity at the cathode inlet ($m\,s^{-1}$)
w	z direction velocity ($m\,s^{-1}$)
W_P	cathode pressure drop loss ($W\,m^{-2}$)
W_r	width of rib (m)
x	x direction coordinate (m)
y	y direction coordinate (m)
z	z direction coordinates (m)
Z_f	species valence

Greek symbols

α_a	electrical transfer coefficient in forward reaction
α_c	electrical transfer coefficient in backward reaction
ε	porosity
ϕ	dependent variables
Φ	phase potential function (V)
η	over-potential (V)
λ	water content in membrane
μ	viscosity (Pa s)
ν	kinematic viscosity ($m^2\,s^{-1}$)
ρ	density ($kg\,m^{-3}$)
σ_m	electric conductivity of membrane
τ	tortuosity of the pores in the porous medium
Ξ_ϕ	exchange coefficient

Superscripts

ref	reference value

Subscripts

a	anode
aver	average
c	cathode
eff	effective
H^+	hydrogen ion
H_2	hydrogen
H_2O	water
in	inlet
k	kth species of the mixture
O_2	oxygen
sat	saturation
total	total

an intermediate channel dimension. Liu et al. [26] investigated the use of baffle-blocked channels to improve reactant transport and cell performance of PEMFCs. Their results indicated that the blockage effects of the baffles forced more reactants through the GDL to enhance the chemical reactions to then augment the cell performance. Shimpalee et al. [27] investigated the effect of the number of gas paths on the reactants transport and cell performance of a 200 cm^2 PEMFC with serpentine flow fields. Kumar and Reddy [28] investigated the effect of the flow field design on the steady and transient state performance of PEMFCs with serpentine, parallel, multiple parallel and discontinuous flow fields. Yan et al. [29] investigated the effects of the flow-field design (parallel flow field, Z-type flow field, serpentine flow field, parallel flow field with baffles and Z-type flow field with baffles) and air flow rate on the cell performance and pressure drop. Yan and co-workers [30,31] proposed a novel straight flow channel with tapered height and width to improve the efficiency of reactant utilization in the PEMFCs. Their results demonstrated that the tapered flow channel increases the reactant velocity which enhances the reactant transport through the porous layers, the reactant utilization, and the liquid water removal. The results also show that the cell performance can be improved by either decreasing the height taper ratio or increasing the width taper ratio. Shimpalee and Van Zee [32] investigated the effects of the channel and rib cross-sectional areas on the reactants distribution and cell performance of 25 cm^2 PEMFCs with serpentine flow fields. They showed that narrower channels with wider rib spacings give higher performance. Wang et al. [33,34] investigated the effect of the flow channel area ratio on the cell performance and local transport characteristics for PEMFCs with parallel and interdigitated flow fields. Wang et al. [35] proposed a novel serpentine-baffle flow field design to improve the cell performance compared that for the conventional serpentine flow field design. They used a three-dimensional model to analyze the corner effect and under-rib convection effect in the cell and found the both effects enhance the oxygen utilization and liquid water removal capability. Yang and Zhao [36] investigated experimentally the effect of the anode flow field design on the performance of direct methanol fuel cells, their results show that both open ratio and flow channel length had significant influ-

ences on the cell performance and pressure drop. An open ratio of around 50% led to the best cell performance at moderate and high methanol solution flow rates. However, at low methanol solution flow rates, a larger open ratio yielded a higher power density at higher current densities, corresponding to the mass transfer limitation region. In addition, it was found that a longer flow channel usually gave better cell performance, but caused a larger pressure drop. Xu and Zhao [37] proposed a new flow field design termed the convection-enhanced serpentine flow field (CESFF), for electrolyte-based fuel cells, obtained by re-patterning the conventional serpentine flow fields (SFFs). Their experimental results showed that the new flow field resulted in substantial improvements in both cell performance and operating stability as opposed to the conventional serpentine flow field design.

The design parameters in the bipolar plates for the SFF design mainly include the active area, cross-sectional shape of the flow channels, widths of the flow channels and ribs, heights of the flow channels and ribs, number of serpentine flow channels and number of flow channel bends. This literature reviews indicates that although there have been some analyses of SFF designs, a systematic, comprehensive study of the effects of the SFF design parameters is still needed. For example, to reduce the computational effort, some studies only simulated a symmetrical unit of the cell which might be reasonable for parallel flow fields, but is not acceptable for the SFF design because the reactant flow in each channel differs and the reactants experience different pressure drops and concentration changes along the channel. For example, for the single SFF shown in Fig. 1, the channel cross-section is small, while the channel length is very long. Then, the pressure drop at neighboring locations between adjacent channels, for example, points a and b in Fig. 1a, would be substantial, thus there is a significant pressure gradient across the porous electrode, much larger than the pressure gradient along the channel direction, resulting in considerable cross-leakage flow between adjacent channels (under-rib convection) [35,37,38]. Therefore, full-cell models are needed to simulate the flow and reactions in the SFF design. This paper describes a study of the flow field design parameters for miniature PEMFCs with the SFF using a three-dimensional, full-cell numerical model. The study focuses on the effects of the number of flow channel bends, number of serpentine loops and the flow channel width ratio on the cell performance, with assumptions of a constant active area and flow channel/rib height and a rectangular flow channel cross-section. The local oxygen mass flow rates, liquid water distributions and local current densities in the cells for various flow fields are examined. The pressure drops are also evaluated for the various SFF designs.

2. Flow channel designs

This paper focuses on miniature PEMFCs. In general, water flooding occurs on the cathode electrode of the PEMFCs, because the electrochemical reaction on the cathode produces water vapor. If the partial pressure of the water vapor is higher than the saturation pressure, the water vapor condenses to form liquid water. When a large amount of liquid water accumulates in the porous layer pores, the oxygen transport resistances increase and oxygen mass flow rates decrease. Therefore, the cathode flow field design is a key factor for enhancing reactant and product transport and removing liquid water. Therefore, the cathode flow field designs are studied in this paper. The anodes for all cells use parallel flow field designs, with 12 flow channels and 11 ribs all with the same heights of 1 mm and the same widths of 1 mm, while the cathodes use serpentine flow field designs with the various design parameters. All cells have rectangular channel cross-sections with 23 mm × 23 mm active areas and the same thicknesses for the GDL, catalyst layer (CL) and membrane (MEM) geometries. All cells have the same flow channel and rib heights of 1 mm. The operating conditions must remain constant for a fair comparison for all cells. The cell temperature is assumed to be 323 K, the reactants on the anode side include hydrogen and water vapor with a relative humidity of 100%, the reactants on the cathode side contain oxygen, nitrogen and water vapor with a relative humidity of 100%, the inlet flow rate on the anode side is 260 $cm^3\ min^{-1}$, the inlet flow rate on the cathode side is 700 $cm^3\ min^{-1}$ and the inlet pressures on the anode and cathode sides are both 1 atm.

The effect of the number of flow channel bends was considered using cell designs with single SFFs with 7, 11 or 15 bends as shown in Fig. 1. To eliminate the effect of the flow channel width ratio, the channel and rib widths were equal for each cell, e.g. channel and rib widths were 1.533 mm for the cell

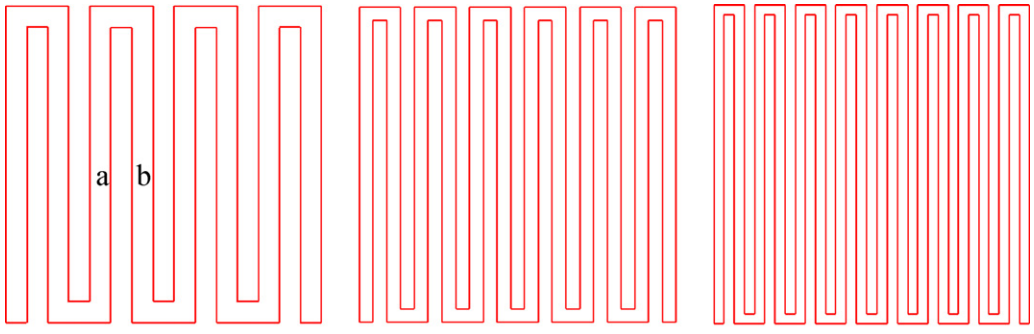

Fig. 1. Schematics of single loop flow fields with various numbers of flow channel bends: (a) 7 bends; (b) 11 bends; (c) 15 bends.

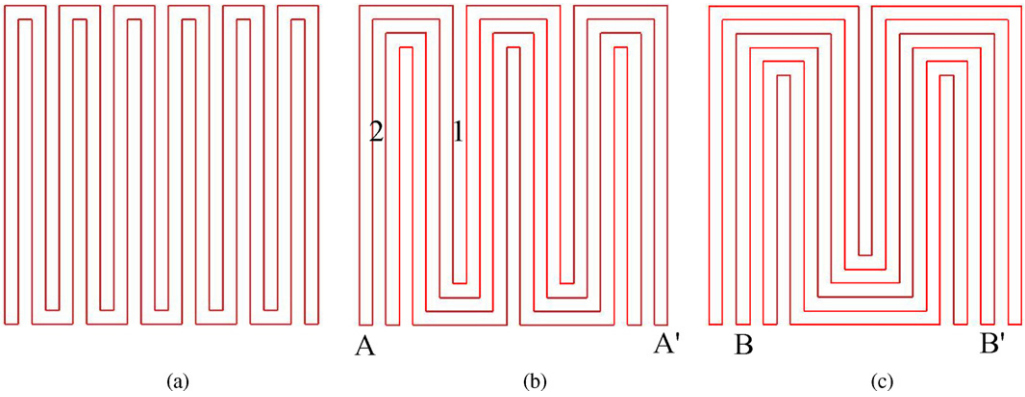

Fig. 2. Schematics of single, double and triple SFFs. (a) Single serpentine; (b) double serpentine; (c) triple serpentine.

Table 1
Physical dimensions of the fuel cell models

Quantity	Value
Reaction area (mm^2)	23×23
Channel height (mm)	1
Rib height (mm)	1
Anode GDL thickness (mm)	0.4
Anode CL thickness (mm)	0.005
Membrane thickness (mm)	0.035
Cathode GDL thickness (mm)	0.005
Cathode CL thickness (mm)	0.4

with 7 bends, 1 mm for the cell with 11 bends and 0.742 mm for the cell with 15 bends. The effect of the number of serpentine loops was analyzed for single, double and triple SFF designs. The channel and rib widths were 1 mm for all three cells, which included 12 channels and 11 ribs as shown in Fig. 2. The effect of the flow channel width ratio was considered for cells with the triple SFF design. The flow channel width ratio, η, was defined as the ratio of the total flow channel width to the total cell width with values of 0.4, 0.522 and 0.6, as shown in Fig. 3, where $\eta = 0.522$ denotes that the flow channel and rib widths are equal (1 mm). Besides these design parameters, all the other parameters, including the thickness, porosity, etc., of the GDL, CL and membrane were the same for all cells. The detailed physical dimensions of the fuel cells are summarized in Table 1.

3. Numerical model

A three-dimensional model was used for the full fuel cell to analyze the electrochemical reactions and transport of the reactants and products. The cell was divided into the anode flow channels, membrane electrode assembly (MEA, including the anode GDL, anode CL, proton exchange membrane, cathode CL and cathode GDL) and the cathode flow channels. The governing equations include the mass, momentum, species and electrical potential conservation equations. The model assumes that the system is three-dimensional and steady, the reactants are ideal gases, the system is isothermal, the flow is laminar, the fluid is incompressible, the thermophysical properties are constant, and the porous layers such as the GDL, CL and proton exchange membrane (PEM) are isotropic.

The transport equations for the three-dimensional PEMFCs are given as:

Continuum equation

$$\frac{\partial u}{\partial x} + \frac{\partial v}{\partial y} + \frac{\partial w}{\partial z} = 0 \tag{1}$$

Momentum equation

$$\varepsilon_{\text{eff}} \left(u\frac{\partial u}{\partial x} + v\frac{\partial u}{\partial y} + w\frac{\partial u}{\partial z} \right) = -\frac{\varepsilon_{\text{eff}}}{\rho}\frac{\partial P}{\partial x} + \nu\varepsilon_{\text{eff}} \left(\frac{\partial^2 u}{\partial x^2} + \frac{\partial^2 u}{\partial y^2} + \frac{\partial^2 u}{\partial z^2} \right) + S_u \tag{2}$$

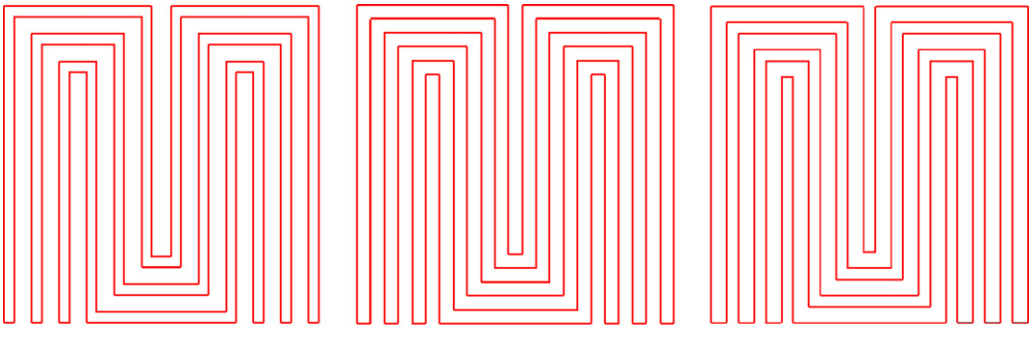

Fig. 3. Schematics of triple SFFs with various flow channel width ratios. (a) $\eta = 0.4$; (b) $\eta = 0.522$; (c) $\eta = 0.6$.

$$\varepsilon_{\text{eff}}\left(u\frac{\partial v}{\partial x}+v\frac{\partial v}{\partial y}+w\frac{\partial v}{\partial z}\right) = -\frac{\varepsilon_{\text{eff}}}{\rho}\frac{\partial P}{\partial y}+\nu\varepsilon_{\text{eff}}\left(\frac{\partial^2 v}{\partial x^2}+\frac{\partial^2 v}{\partial y^2}+\frac{\partial^2 v}{\partial z^2}\right)+S_v \quad (3)$$

$$\varepsilon_{\text{eff}}\left(u\frac{\partial w}{\partial x}+v\frac{\partial w}{\partial y}+w\frac{\partial w}{\partial z}\right) = -\frac{\varepsilon_{\text{eff}}}{\rho}\frac{\partial P}{\partial z}+\nu\varepsilon_{\text{eff}}\left(\frac{\partial^2 w}{\partial x^2}+\frac{\partial^2 w}{\partial y^2}+\frac{\partial^2 w}{\partial z^2}\right)+S_w \quad (4)$$

Species equation

$$\varepsilon_{\text{eff}}\left(u\frac{\partial C_k}{\partial x}+v\frac{\partial C_k}{\partial y}+w\frac{\partial C_k}{\partial z}\right) = D_{k,\text{eff}}\left(\frac{\partial^2 C_k}{\partial x^2}+\frac{\partial^2 C_k}{\partial y^2}+\frac{\partial^2 C_k}{\partial z^2}\right)+S_{\text{c}}+S_{\text{L}} \quad (5)$$

In the momentum equation, ε is the porosity and S_u, S_v and S_w are the corrected terms of the reactant flow in the gas diffusion layer and the catalyst layer and of the proton transfer in the PEM, which is listed in Table 2. In the species equation, $D_{k,\text{eff}}$ is the effective diffusion coefficient and S_{c} represents the source terms due to the chemical reaction in the catalyst layer and the proton exchange membrane. The Bruggeman correction [23] is employed to describe the influence of the porosity on the diffusion coefficient

$$D_{k,\text{eff}} = D_k\varepsilon^{\tau} \quad (6)$$

If the partial pressure of water vapor is greater than the saturation pressure, the liquid water forms in the PEMFC. To consider the effect of the liquid water formation, it is assumed that the pore in the porous material is blocked by liquid water, which results in the modification of the diffusion coefficient and the porosity in the species equation. The source term S_{L} in the species equation due to the liquid water is determined by [14]

$$S_{\text{L}} = \begin{cases} M_{\text{H}_2\text{O}}k_{\text{c}}\dfrac{\varepsilon_{\text{eff}}C_{\text{H}_2\text{O}}}{\rho RT}(P_{\text{H}_2\text{O}}-P_{\text{sat}}), & \text{if } P_{\text{H}_2\text{O}} > P_{\text{sat}} \\ k_{\text{e}}\varepsilon_{\text{eff}}s(P_{\text{sat}}-P_{\text{H}_2\text{O}}), & \text{if } P_{\text{H}_2\text{O}} < P_{\text{sat}} \end{cases} \quad (7)$$

where the saturation s is the ratio of the liquid water volume to pore volume in the porous material, M the molecular weight of water, k_{c} the condensation rate constant of water, k_{e} the evaporation rate constant of water and ε_{eff} is the modified effective porosity of the porous medium by considering the liquid water effect which is given by

$$\varepsilon_{\text{eff}} = \varepsilon(1-s) \quad (8)$$

The saturation pressure of water can be expressed as

$$P_{\text{sat}} = 10^{-2.1794+0.02953T-9.1837\times10^{-5}T^2+1.4454\times10^{-7}T^3} \quad (9)$$

Table 2
Source terms in the governing equations

	S_u	S_v	S_w	S_{c}
Channel	0	0	0	–
GDL	$-\frac{\nu\varepsilon_{\text{eff}}^2}{k_{\text{p}}}u-\frac{\varepsilon_{\text{eff}}^3C_{\text{F}}\rho u}{\sqrt{k_{\text{p}}}}\sqrt{u^2+v^2+w^2}$	$-\frac{\nu\varepsilon_{\text{eff}}^2}{k_{\text{p}}}v-\frac{\varepsilon_{\text{eff}}^3C_{\text{F}}\rho v}{\sqrt{k_{\text{p}}}}\sqrt{u^2+v^2+w^2}$	$-\frac{\nu\varepsilon_{\text{eff}}^2}{k_{\text{p}}}w-\frac{\varepsilon_{\text{eff}}^3C_{\text{F}}\rho w}{\sqrt{k_{\text{p}}}}\sqrt{u^2+v^2+w^2}$	0
CL	$-\frac{\nu\varepsilon_{\text{eff}}^2}{k_{\text{p}}}u-\frac{\varepsilon_{\text{eff}}^3C_{\text{F}}\rho u}{\sqrt{k_{\text{p}}}}\sqrt{u^2+v^2+w^2}$	$-\frac{\nu\varepsilon_{\text{eff}}^2}{k_{\text{p}}}v-\frac{\varepsilon_{\text{eff}}^3C_{\text{F}}\rho v}{\sqrt{k_{\text{p}}}}\sqrt{u^2+v^2+w^2}$	$-\frac{\nu\varepsilon_{\text{eff}}^2}{k_{\text{p}}}w-\frac{\varepsilon_{\text{eff}}^3C_{\text{F}}\rho w}{\sqrt{k_{\text{p}}}}\sqrt{u^2+v^2+w^2}$	$\text{H}_2: -\frac{1}{2FC_{\text{total,a}}}j_{\text{a}}$, $\quad \text{O}_2: -\frac{1}{4FC_{\text{total,c}}}j_{\text{c}}$, $\text{H}_2\text{O}: \frac{1}{2FC_{\text{total,c}}}j_{\text{c}}$
Membrane	$-\frac{\nu\varepsilon_{\text{eff}}^2}{k_{\text{p}}}u-\frac{\varepsilon_{\text{eff}}^3C_{\text{F}}\rho u}{\sqrt{k_{\text{p}}}}\sqrt{u^2+v^2+w^2}$ $+\frac{k_{\text{p}}}{\nu}Z_{\text{f}}C_{\text{H}^+}F\nabla\Phi u_x$	$-\frac{\nu\varepsilon_{\text{eff}}^2}{k_{\text{p}}}v-\frac{\varepsilon_{\text{eff}}^3C_{\text{F}}\rho v}{\sqrt{k_{\text{p}}}}\sqrt{u^2+v^2+w^2}$ $+\frac{k_{\text{p}}}{\nu}Z_{\text{f}}C_{\text{H}^+}F\nabla\Phi v_y$	$-\frac{\nu\varepsilon_{\text{eff}}^2}{k_{\text{p}}}w-\frac{\varepsilon_{\text{eff}}^3C_{\text{F}}\rho w}{\sqrt{k_{\text{p}}}}\sqrt{u^2+v^2+w^2}$ $+\frac{k_{\text{p}}}{\nu}Z_{\text{f}}C_{\text{H}^+}F\nabla\Phi w_z$	$\frac{ZF}{RT}D_{k,\text{eff,H}^+}C_{\text{H}^+}\left(\frac{\partial^2\Phi}{\partial x^2}+\frac{\partial^2\Phi}{\partial y^2}+\frac{\partial^2\Phi}{\partial z^2}\right)$

To calculate the local current density, the phase potential equations should be solved

$$\frac{\partial}{\partial x}\left(\sigma_{\mathrm{m}}\frac{\partial \Phi}{\partial x}\right)+\frac{\partial}{\partial y}\left(\sigma_{\mathrm{m}}\frac{\partial \Phi}{\partial y}\right)+\frac{\partial}{\partial z}\left(\sigma_{\mathrm{m}}\frac{\partial \Phi}{\partial z}\right)=S_j \tag{10}$$

where $S_j=0$ in the membrane, $S_j=-j_{\mathrm{a}}$ in the anode catalyst layer, $S_j=j_{\mathrm{c}}$ in the cathode catalyst layer, Φ the phase potential and σ_{m} is the ionic conductivity of the membrane. In this study, Butler–Volmer equation [7] is used to calculate the transfer current density generated by the electrochemical reaction

$$j_{\mathrm{a}}=Aj_{0,\mathrm{a}}^{\mathrm{ref}}\left(\frac{C_{\mathrm{H_2}}}{C_{\mathrm{H_2}}^{\mathrm{ref}}}\right)\left[\mathrm{e}^{(\alpha_{\mathrm{a}}F/RT)\eta}-\frac{1}{\mathrm{e}^{(\alpha_{\mathrm{c}}F/RT)\eta}}\right] \tag{11}$$

$$j_{\mathrm{c}}=Aj_{0,\mathrm{c}}^{\mathrm{ref}}\left(\frac{C_{\mathrm{O_2}}}{C_{\mathrm{O_2}}^{\mathrm{ref}}}\right)\left[\mathrm{e}^{(\alpha_{\mathrm{a}}F/RT)\eta}-\frac{1}{\mathrm{e}^{(\alpha_{\mathrm{c}}F/RT)\eta}}\right] \tag{12}$$

where Aj_0^{ref} is the reference exchange current density, α_{a} and α_{c} the transfer coefficient in anode and cathode catalyst layers, η the over-potential, R the gas constant and T is the temperature of the fuel cell. The ionic conductivity of the membrane can be calculated by [2]

$$\sigma_{\mathrm{m}}(T)=\sigma_{\mathrm{m}}^{\mathrm{ref}}\exp\left[1268\left(\frac{1}{303}-\frac{1}{T}\right)\right] \tag{13}$$

and the reference ionic conductivity is

$$\sigma_{\mathrm{m}}^{\mathrm{ref}}=0.005139\lambda-0.00326 \tag{14}$$

$$\lambda=\begin{cases}0.043+17.81a-39.85a^2+36.0a^3, & 0\le a\le 1\\ 14+1.4(a-1), & 1<a\le 3\end{cases} \tag{15}$$

where a is the activity of water vapor at the cathode side. The relationship between the phase potential and the current density is given by

$$i_x=-\sigma_{\mathrm{m}}\frac{\partial \Phi}{\partial x} \tag{16}$$

$$i_y=-\sigma_{\mathrm{m}}\frac{\partial \Phi}{\partial y} \tag{17}$$

$$i_z=-\sigma_{\mathrm{m}}\frac{\partial \Phi}{\partial z} \tag{18}$$

Boundary conditions at the anode flow channels and the cathode flow channels are as follows: the inlet flow rates are constant, the inlet gas compositions are constant and the flows are fully developed at the outlets of the anode and cathode flow channels. At the solid walls, no slip and zero fluxes are hold. At the interfaces between the gas channels, the diffuser layers, the catalyst layers and the PEM, equalities of the velocity, mass fraction, momentum flux and mass flux are applied. More details were given elsewhere [31]. Main parameters used in the model are listed in Table 3.

The model uses non-uniformly distributed elements with 116, 93 and 33 elements in the x, y and z directions (the flow channel inlets are along the y direction, and the cell height is along the z direction). The grid independence was examined in preliminary test runs. Four non-uniformly distributed grid configurations were evaluated for PEMFC with the parallel flow channel design. The numbers of elements in the x, y and z directions were: (I) $70\times70\times25$, (II) $93\times93\times33$, (III) $116\times93\times33$ and (IV) $116\times116\times41$. The influence of the number of elements on the local current density distributions at the operating voltage of 0.3 V for the fuel cell with parallel flow field is shown in Fig. 4. The local current density distribution for grid (I) differs from those for grids (II–IV) with the deviation about 3.9%. However, the local current density distributions for grids (II), (III) and (IV) do not show any notable differences. The difference between the local current densities for (II) and (III) is about 0.32% and the difference between (III) and (IV) is about 0.25%. Grid (III) was chosen for the simulations as a tradeoff between accuracy and execution time.

Table 3
Fuel cell parameters

Parameter	Value
$Aj_{0,\mathrm{a}}^{\mathrm{ref}}$ (A m^{-3})	9×10^8
$Aj_{0,\mathrm{c}}^{\mathrm{ref}}$ (A m^{-3})	1.5×10^2
α_{a}	0.5
α_{c}	1.5
$\varepsilon_{\mathrm{channel}}$	1
τ_{channel}	1
k_{channel} (m^2)	∞
$\varepsilon_{\mathrm{GDL}}$	0.5
τ_{GDL}	1.5
k_{GDL} (m^2)	1.76×10^{-10}
$\varepsilon_{\mathrm{CL}}$	0.4
τ_{CL}	1.5
k_{CL} (m^2)	1.76×10^{-11}
$\varepsilon_{\mathrm{Mem}}$	0.28
τ_{Mem}	Dagan model
k_{Mem} (m^2)	1.8×10^{-18}

In the present paper, the oxygen mass flow rates and liquid water distributions on the cathode GDL–CL interface at the two representative operating voltages of 0.3 and 0.7 V are analyzed to understand the effects of the various flow field designs on the cell performance. For cells with various numbers of flow channel bends and cells with various numbers of serpentine loops, the local transport phenomena in the entire cell were analyzed by

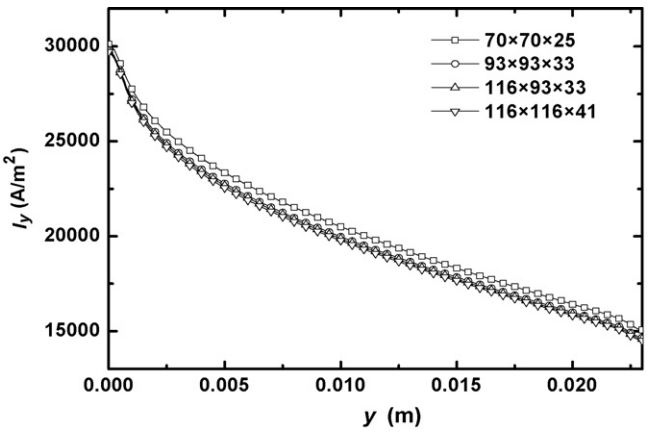

Fig. 4. Influence of number of elements on the local current densities on middle cross-section in the PEM at the operating voltage of 0.3 V.

plotting all local physical quantities along a specified serpentine channel from the inlet to the outlet. For the double SFF the data was plotted along the AA′ serpentine loop while for the triple SFF, the data was plotted along the BB′ serpentine loop (as shown in Fig. 2b and c). However, when analyzing the effect of the flow channel width ratio, the data was plotted at $y = 11.5$ mm.

4. Results and discussions

4.1. Effect of number of flow channel bends

Fig. 5 presents the I–V_{cell} polarization curves and I–W_{cell} power density curves for single SFFs with the various number of flow channel bends. When the operating voltage is greater than 0.7 V, the I–V_{cell} curves and I–W_{cell} curves for all cells with the various numbers of flow channel bends almost coincide, indicating that the cell performance is not dependent on the number of bends because at the higher operating voltages the electrochemical reaction rate is lower with a small amount of oxygen consumption and liquid water, thus the cells with the various numbers of bends all provide sufficient oxygen to satisfy the needs of the electrochemical reaction. As the operating voltage decreases, the current density gradually increases and the cell performance for the various numbers of bends starts to differ. As the number of bends increases, the limiting current density and cell output power density increase and the cell performance improves.

Fig. 6 presents the local oxygen mass flow rates across the cathode GDL–CL interface at the operating voltages of 0.3 and 0.7 V for the various number of bends, where L denotes the distance measured from the flow channel inlet. Fig. 6 shows that at the high operating voltage of 0.7 V, the oxygen mass flow rates are almost unchanged along the flow direction and are almost equal for the three different numbers of flow channel bends. Since the oxygen mass flow rate on the cathode GDL–CL interface is equal to the oxygen consumed by the electrochemical reaction in the CL, then the number of flow channel bends has little effect on the cell performance at high operating voltages. At the low operating voltage of 0.3 V, the oxygen mass flow rates are all greater than those at the high operating voltage of 0.7 V for the three different numbers of flow channel bends, indicating that at the low operating voltages the electrochemical reactions are

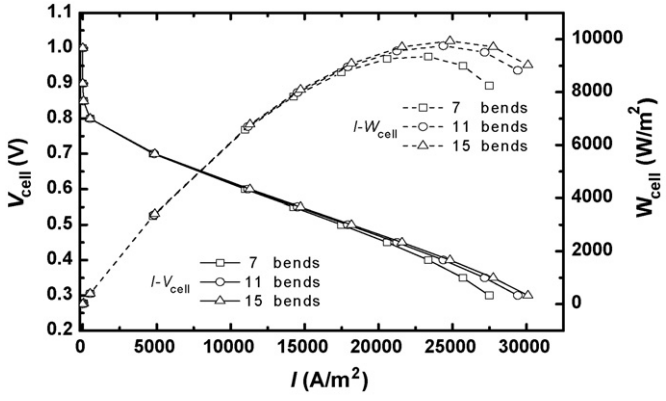

Fig. 5. Effect of number of flow channel bends on cell performance.

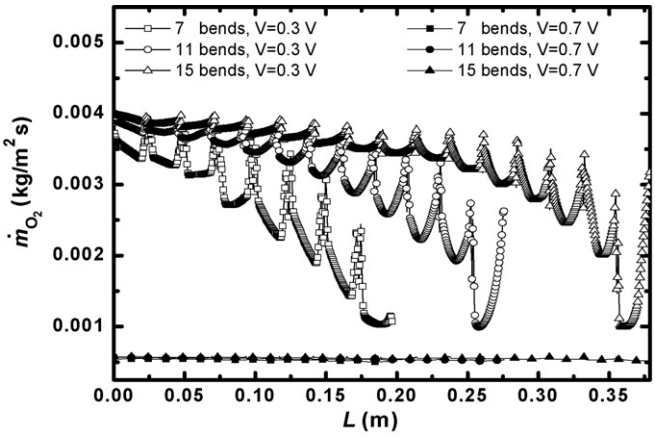

Fig. 6. Oxygen mass flow rates on cathode GDL–CL interface at operating voltages of 0.3 and 0.7 V for single loop flow fields with 7, 11 and 15 bends.

stronger with more oxygen consumption. For all three numbers of flow channel bends, the maximum oxygen mass flow rates occur at the inlet and gradually decrease towards the outlet, with local peaks at the bends of the flow channels. The inlet oxygen concentration is the highest, thus the largest oxygen mass flow rates through the GDL–CL interface will occur near the inlet. Then, the oxygen is gradually consumed by the electrochemical reaction, so the oxygen concentration gradually decreases along the flow direction and, thus, the oxygen mass flow rate across the GDL–CL interface gradually decreases. At the channel bends, the corners of flow channels force the reactants to flow into the GDL and CL; thus, the oxygen mass flow rate through the GDL–CL interface sharply increases at the bends. Fig. 6 also indicates that at the same L, the oxygen mass flow rate increases as the number of flow channel bends increases because cells with larger numbers of bends have smaller flow channel cross-sectional areas; thus, at the same reactants inlet mass flow rates, the reactants inlet velocity higher. Furthermore, a larger number of flow channel bends means that there are more corners in the channels, which forces more oxygen flow into the GDL to increase the local oxygen mass flow rate. Therefore, increasing the number of flow channel bends enhances the oxygen utilization efficiency.

The electrochemical reaction in PEM fuel cells produces water vapor, which normally condenses since the normal operating temperatures are between 40 and 80 °C. However, liquid water then increases the resistance to fuel transport into the catalyst layer, resulting in reduced cell performance. Fig. 7 presents the liquid water distributions on the cathode GDL–CL interface at operating voltages of 0.3 and 0.7 V for the various numbers of flow channel bends. The results indicate that the liquid water concentration at the high operating voltage of 0.7 V is less than at the low operating voltage of 0.3 V because at the high operating voltage of 0.7 V the electrochemical reaction is weaker with less production of liquid water. At the low operating voltage of 0.3 V, the liquid water concentrations gradually increase along the flow direction, while reach the local minimum values at the bends of the flow channel. Although more liquid water is produced in the porous layers near the flow channel inlets due to the stronger electrochemical reaction rates, the high local

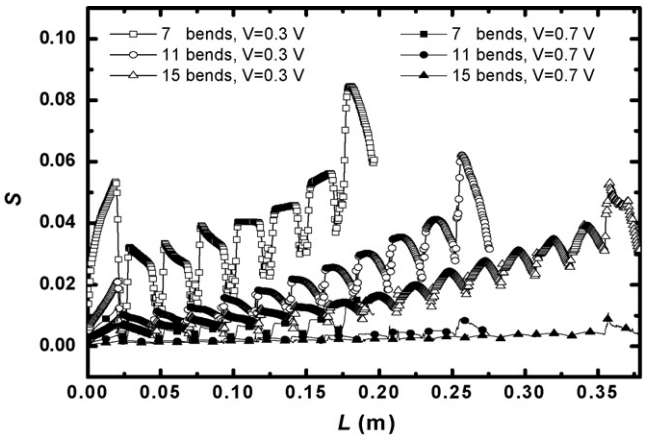

Fig. 7. Liquid water concentrations on cathode GDL–CL interface at operating voltages of 0.3 and 0.7 V for single loop flow fields with 7, 11 and 15 bends.

oxygen mass flow rates in the porous layers generate high shear forces which carry the liquid water downstream to the flow channel, so the liquid water concentrations gradually increase along the flow direction. However, at the bends of the flow channels, the corners force the reactants to enter the porous layers which enhances the liquid water removal; thus, local minimums appear in the liquid water distributions at the bends. At low operating voltages, the electrochemical reaction produces large amounts of liquid water. If the liquid water is not removed but accumulates in the pores of the GDL and CL, the oxygen transport resistances increase, which reduces the electrochemical reaction rate. Fig. 7 shows that the liquid water concentrations with 15 flow channel bends is much lower than for 11 and 7 flow channel bends, because it has a higher oxygen mass flow rate. Thus, a proper flow field design can effectively enhance the reactant transport rates and liquid water removal, which both improve cell performance.

4.2. Effect of number of serpentine loops

Fig. 8 shows the I–V_{cell} polarization curves and I–W_{cell} power density curves for the single, double and triple loop flow fields. Fig. 8 shows that as for operating voltages greater than 0.7 V, the number of serpentine loops has little effect on the cell performance. As the operating voltage decreases, the number of serpentine loops begins to affect the cell performance with the single SFF design having better performance than the double and triple flow field designs.

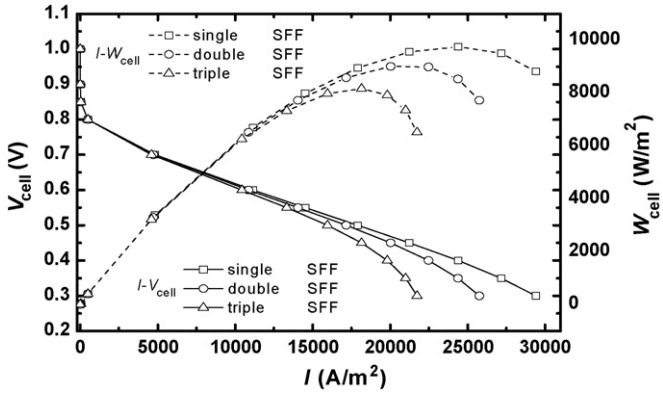

Fig. 8. Effect of number of flow channel serpentine loops on cell performance.

Fig. 9 shows the oxygen mass flow rates on the cathode GDL–CL interface at the operating voltages of 0.3 and 0.7 V for the various numbers of serpentine loops. Fig. 9 shows that at the higher operating voltage of 0.7 V, the oxygen mass flow rates are almost equal and unchanged along the flow direction for the single, double, and triple SFF designs, so the cell performance is not dependent on the number of serpentine loops. At the lower operating voltage of 0.3 V, the maximum oxygen mass flow rates for all three flow field designs all occur at the inlet and then gradually decrease towards the outlet. The oxygen mass flow rates have local maximums at the bends in the flow channels for the same reason as given in Section 4.1. Fig. 9 also shows that at the same L, the oxygen mass flow rates increase with decreasing number of serpentine loops because as the number of loops decreases the reactant inlet velocity increases. Compared with the parallel flow field configuration where the reactants only enter the porous layers by diffusion, in the loop design the reactants are also forced into the GDL by the flow field design which creates under-rib convection. The under-rib convection can significantly enhance the local oxygen mass flow rates in the porous layers under the ribs. For the single SFF design, the under-rib convection occurs between all the ribs, while for the double and triple SFF designs, under-rib convection only occurs at the specified ribs. For example, under-rib convection occurs at rib 1 in Fig. 2b, but not at rib 2 in Fig. 2b. Therefore, the reactant utilization for the single serpentine flow field is higher than for double and triple serpentine flow field designs.

Fig. 10 shows the liquid water distributions on the cathode GDL–CL interface at the operating voltages of 0.3 and 0.7 V for the various numbers of serpentine loops. The liquid water distributions are opposite to the oxygen mass flow rate distributions, as discussed in Section 4.1. The single flow loop enhances the reactant utilization and liquid water removal, so it has the best cell performance.

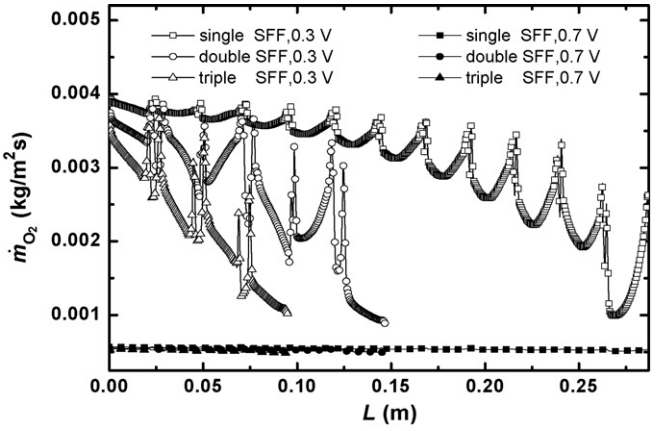

Fig. 9. Oxygen mass flow rates on cathode GDL–CL interface at operating voltages of 0.3 and 0.7 V for single, double and triple loop flow fields.

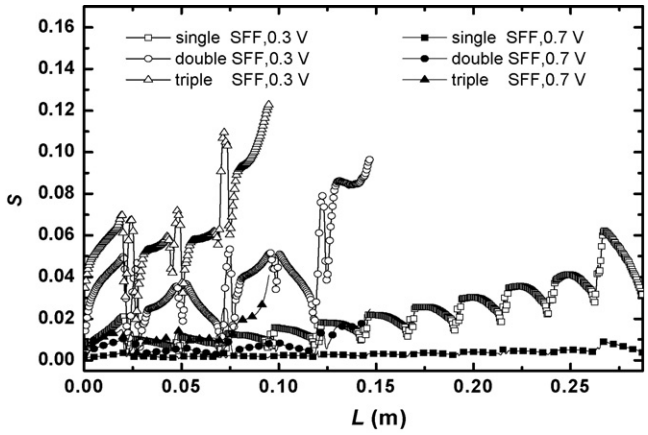

Fig. 10. Liquid water concentrations on cathode GDL–CL interface at operating voltages of 0.3 and 0.7 V for single, double and triple loop flow fields.

4.3. Effect of flow channel width ratio

Fig. 11 shows the I–V_{cell} polarization curves and I–W_{cell} power density curves for the various flow channel width ratios. The results show that for operating voltages greater than 0.7 V, the effect of the flow channel width ratio on the cell performance can be neglected. At the lower operating voltages, the cell performance improves slightly as the flow channel width ratio increases, indicating that the cell performance is not strongly related to the flow channel width ratio for PEMFCs with the SFF design. For the parallel flow field design, as the flow channel width ratio increases the cell performance significantly improves because the reactants are transported into the GDL and CL mainly by diffusion. A larger flow channel width ratio increases the contact area between the reactants and the GDL, which allows more reactants to directly diffuse into the porous layers to participate in the electrochemical reaction which enhances the reaction rates [33]. However, for the SFF design, the reactants enter the GDL by forced convection at the flow channel bends due to the corners as well as diffusion. In addition, there is also the under-rib convection [35,37,38] between adjacent flow channels. The forced convection and the under-rib convection significantly enhance the local oxygen mass flow rates in the porous layers, so the flow channel width ratio has less effect in the SFF design.

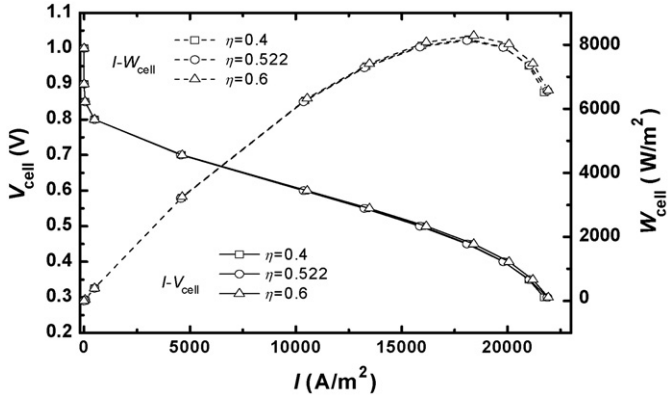

Fig. 11. Effect of flow channel width ratio on cell performance.

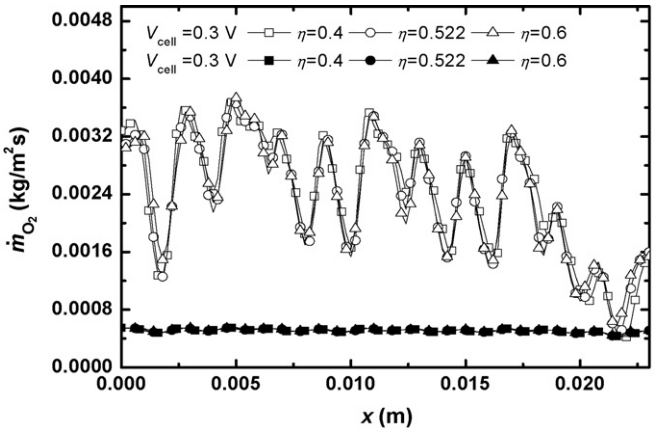

Fig. 12. Oxygen mass flow rates at $y = 11.5$ mm on cathode GDL–CL interface at operating voltages of 0.3 and 0.7 V for triple loop flow fields with various flow channel width ratios.

Figs. 12 and 13 show the oxygen mass flow rates and liquid water distributions at $y = 11.5$ mm on the cathode GDL–CL interface at the operating voltages of 0.3 and 0.7 V for the various flow channel width ratios. The liquid water distribution is opposite to the oxygen mass flow rate distribution. At the higher operating voltage of 0.7 V, the oxygen mass flow rates and liquid water concentrations, are lower than those at the lower operating voltage of 0.3 V, with their values almost equal to each other for the three flow channel width ratios, so the cell performance is not dependent on the flow channel width ratio. At the lower operating voltage of 0.3 V, as the flow channel width ratio increases, the oxygen mass flow rates increase slightly, while the liquid water concentrations decreases slightly, so the cell performance improves a little.

4.4. Pressure drop losses

The flow field design influences not only the cell performance but also the pressure drop in the fuel cell. Larger pressure drops

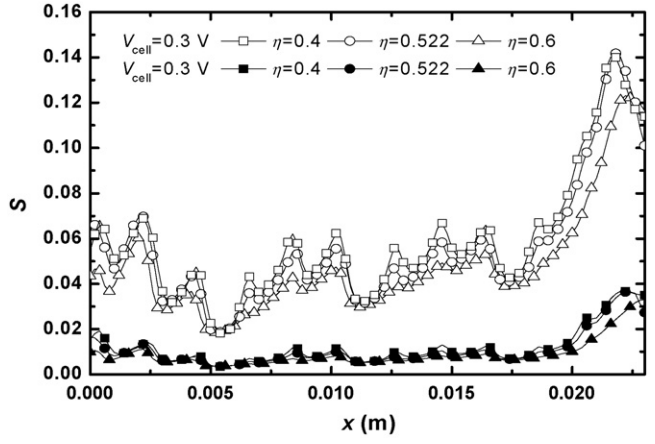

Fig. 13. Liquid water concentrations at $y = 11.5$ mm on cathode GDL–CL interface at operating voltages of 0.3 and 0.7 V for triple loop flow fields with various flow channel width ratios.

Table 4
Estimated pressure drop losses at 0.3 V

Flow field types	ΔP (Pa)	W_{cell} (W m^{-2})	W_P (W m^{-2})	W_{net} (W m^{-2})
Single SFF with 7 bends	671	8245.52	14.80	8230.72
Single SFF with 11 bends	1384	8820.99	30.52	8790.47
Single SFF with 15 bends	1853	9027.16	40.88	8986.28
Double SFF	927	7727.30	10.22	7717.08
Triple SFF with $\eta = 0.4$	1002	6519.46	7.37	6512.07
Triple SFF with $\eta = 0.522$	608	6564.96	4.47	6560.49
Triple SFF with $\eta = 0.6$	470	6577.37	3.46	6573.91

in the fuel cell mean that more power is needed to pump the reactants. Thus, the pressure drop is a significant issue to be considered in choosing the flow field designs in addition to the I–V_{cell} curve. The cathode pressure drop has been converted to a power density using [21]:

$$W_P = \frac{\Delta P A_{channel} V}{A_{total}} \quad (19)$$

where W_P represents the cathode pressure drop loss, ΔP the total cathode pressure drop in the fuel cell, $A_{channel}$ the cathode cross-sectional flow inlet area, V the fuel velocity at the cathode inlet and A_{total} represents the total reaction area. Table 4 lists the pressure drop losses for all the flow fields discussed in this paper. As the number of flow channel bends increases and the number of serpentine loops decreases, the total pressure drops and pressure drop losses increase, but the pressure drop losses are far less than the cell output power, W_{cell}, for the miniature PEMFCs due to their small flow channel cross-sectional areas and low reactant inlet velocities. Therefore, the pressure drop losses can be neglected.

5. Conclusions

Appropriate flow channel design is an effective means for improving cell performance. A three-dimensional numerical model was used to analyze the effects of various design parameters for the bipolar plates on the cell performance and local transport phenomena for PEMFCs with the serpentine flow field design. The results indicate that:

1. At high operating voltages, the various bipolar plate design parameters have little effect on the cell performance.
2. At low operating voltages, the design parameters significantly affect the cell performance. For the single serpentine loop flow field, the cell performance improves as the number of flow channel bends increases. The single serpentine flow loop field has better performance than the double and triple loop flow fields. The flow channel width ratio, η, has a relatively small effect on the cell performance, with the best performance for $\eta = 0.6$.
3. Although the pressure drops differ for the various flow field designs, the pressure drop losses can be neglected for the miniature PEMFCs because the pressure drop losses are far less than the cell output power.

Acknowledgement

This study was supported by the National Natural Science Foundation of China (No. 50636020).

References

[1] D.N. Bernadi, M.W. Verbrugge, AIChE J. 37 (1991) 1151.
[2] T.E. Springer, T.A. Zawodizinski, S. Gottesfeld, J. Electrochem. Soc. 138 (1991) 2334.
[3] V. Gurau, F. Barbir, H. Liu, J. Electrochem. Soc. 47 (2000) 2468.
[4] H.V. Bussel, F. Koene, R. Mallant, J. Power Sources 71 (1998) 218.
[5] D. Singh, D.M. Lu, N. Djilali, Int. J. Eng. Sci. 37 (1999) 431.
[6] J.S. Yi, T.V. Nguyen, J. Electrochem. Soc. 145 (1998) 1149.
[7] V. Gurau, H. Liu, S. Kakac, AIChE J. 44 (1998) 2410.
[8] J.S. Yi, T.V. Nguyen, J. Electrochem. Soc. 146 (1999) 38.
[9] I.M. Hsing, P. Futerko, Chem. Eng. Sci. 55 (2000) 4209.
[10] S.H. Ge, B.L. Yi, J. Power Sources 124 (2003) 1.
[11] W.M. Yan, C.Y. Soong, F. Chen, H.S. Chu, J. Power Sources 125 (2004) 27.
[12] S. Dutta, S. Shimpalee, J.W. Van Zee, Int. J. Heat Mass Transfer 44 (2001) 2029.
[13] S. Mazumder, J.V. Cole, J. Electrochem. Soc. 150 (2003) A1503.
[14] S. Mazumder, J.V. Cole, J. Electrochem. Soc. 150 (2003) A1510.
[15] S. Um, C.Y. Wang, J. Power Sources 125 (2004) 40.
[16] T.V. Nguyen, R.E. White, J. Electrochem. Soc. 140 (1993) 2178.
[17] T. Okada, X. Gang, M. Meeg, Electrochim. Acta 43 (14/15) (1998) 2141.
[18] T. Okada, G. Xie, O. Gorseth, S. Kjelstrup, N. Nakamura, T. Arimura, Electrochim. Acta 43 (1998) 3741.
[19] J.J. Baschuk, X. Li, J. Power Sources 86 (2000) 181.
[20] A. Kazim, H.T. Liu, P. Forges, J. Appl. Electrochem. 29 (1999) 1409.
[21] M. Hu, A. Gu, M. Wang, X. Zhu, L. Yu, Energy Convers. Manage. 45 (2004) 1861.
[22] M. Hu, A. Gu, M. Wang, X. Zhu, L. Yu, Energy Convers. Manage. 45 (2004) 1883.
[23] W. He, J.S. Yi, T.V. Nguyen, AIChE J. 46 (10) (2000) 2053.
[24] T.V. Nguyen, J. Electrochem. Soc. 143 (1996) L103.
[25] S.W. Cha, R. O'Hayre, Y. Satio, F.B. Prinz, J. Power Sources 134 (2004) 57.
[26] H.C. Liu, W.M. Yan, C.Y. Soong, F. Chen, J. Power Sources 142 (2005) 125.
[27] S. Shimpalee, S. Greenway, J.W. Van Zee, J. Power Sources 160 (2006) 398.
[28] A. Kumar, R.G. Reddy, J. Power Sources 155 (2006) 264.
[29] W.M. Yan, H.Y. Li, W.C. Tsai, J. Electrochem. Soc. 153 (2006) A1984.
[30] H.C. Liu, W.M. Yan, C.Y. Soong, F. Chen, H.S. Chu, J. Power Sources 158 (2006) 78.
[31] W.M. Yan, H.C. Liu, C.Y. Soong, F. Chen, C.H. Cheng, J. Power Sources 161 (2006) 907.

[32] S. Shimpalee, J.W. Van Zee, Int. J. Hydrogen Energy 32 (2007) 842.
[33] X.D. Wang, Y.Y. Duan, W.M. Yan, J. Power Sources 172 (2007) 265.
[34] H.C. Liu, W.M. Yan, X.D. Wang, J. Electrochem. Soc., 154 (12) (2007), in press.
[35] X.D. Wang, Y.Y. Duan, W.M. Yan, J. Power Sources 173 (2007) 210.
[36] H. Yang, T.S. Zhao, Electrochim. Acta 50 (2005) 3243.
[37] C. Xu, T.S. Zhao, Electrochem. Commun. 9 (2007) 497.
[38] T. Kanezaki, X. Li, J.J. Baschuk, J. Power Sources 162 (2006) 415.